Aerodynamic ground effect at noncontinuum conditions

R. Shapiro and A. Manela ** The Stephen B. Klein Faculty of Aerospace Engineering, Technion-Israel Institute of Technology, Haifa 3200003, Israel



(Received 15 December 2024; accepted 2 September 2025; published 18 September 2025)

We analyze the impact of gas rarefaction on the two-dimensional aerodynamic ground effect over a flat plate. Focusing on highly rarefied flow conditions, we formulate the free-molecular problem based on the collisionless Boltzmann equation and the Maxwell boundary conditions. A semianalytical solution is derived, where specular and diffuse surface reflections are studied separately. The calculated ballistic field is compared with direct simulation Monte Carlo computations at finite Knudsen numbers to test its validity and breakdown with decreasing rarefaction. The specific effect of ground reflections is illustrated through comparison with the nonconfined (in the absence of ground) flow field. The results indicate that the ground invariably increases the aerodynamic loading on the plate and shifts the maximum lift value to lower angles of attack compared with the nonconfined configuration. While the ground may yield a negative contribution to the lift in the continuum (ideal-flow) limit, its relative difference compared with the nonconfined setup is found significantly larger and consistently positive at high Knudsen numbers.

DOI: 10.1103/kj7s-rhth

I. INTRODUCTION

The aerodynamic ground effect, concerning the effect of the ground on the aerodynamic loadings over a flying vehicle, has been studied in detail over the years in continuum aerodynamics. Either for the purpose of estimating the impact of ground upon takeoff or landing, or for exploring the possibility of using aerodynamic forces to promote high-speed ground transportation, the problem has been explored since the beginning of the previous century. Starting with wind tunnel [1,2] and flight test [3] experiments, and continuing to theoretical (potential-flow-based) investigations of the two- and three-dimensional inviscid incompressible problem [4–6], the ground effect was explored in various aerodynamic configurations, including the canonical flat plate and other cambered structures. Later works considered the more involved viscous problem, implementing heavy-load numerical schemes for the calculation of the flow field and loading over aerodynamic objects [7-10].

Rarefied gas aerodynamics has been studied since the 1950s, analyzing single-airfoil aerodynamic performance at free-stream conditions. To this end, Stadler and Zurick [11] were among the first to consider the problem, investigating the free-molecular loading on several aerodynamic configurations. Focusing on a flat-plate geometry, later works have followed, examining effects such as surface conditions [12], gas rarefaction rates [13–16], and thermal wall properties [17] on the structure aerodynamic properties. Additional studies have analyzed other airfoil geometrical configurations, investigating their surrounding free-stream flow properties [18-20]. These works rely mainly on numerical calculations, including the direct simulation Monte Carlo (DSMC) method, model presentations of the Boltzmann equation, or continuum-limit-based solvers. In a

^{*}Contact author: amanela@technion.ac.il

recent contribution, the rarefied-gas wind tunnel problem was considered, studying the highly rarefied pressure-driven gas flow over a flat plate placed in a two-dimensional channel [21].

To date, ground effect investigations have been limited to the continuum regime only. However, in cases where noncontinuum conditions prevail, such analyses cannot be followed to predict the correct aerodynamic behavior. Specifically, body motions in the vicinity of confining surfaces at noncontinuum conditions are encountered in a variety of applications. These include landing and takeoff scenarios over rarefied-atmosphere planets, where the typical flight velocities are of the order of a few meters per second and the molecular mean free paths are of the order of decimeters and above [22]. Prominently, the mean free path in the lunar atmosphere is of the order of 1 m [23], and similar values are found over Io (Jupiter I) [24] and Europa (Jupiter II) [25] planet surfaces. In a different context, the noncontinuum ground effect becomes significant in the design of novel transportation means, such as the Hyperloop [26]. Composed as a sealed tube through which a pod vehicle at near-vacuum conditions is set into motion, the effect of the confining facility on the Hyperloop aerodynamic efficiency is evident. In this context, several investigations on rarefied gas flows over airfoil-shaped surfaces have been carried out, specifically for the Hyperloop configuration [27,28], as well as for examining the coupling between the dynamic and thermodynamic gas states (e.g., Ref. [20]). In a third set of applications, the levitation and control of objects motions at near-vacuum conditions in the vicinity of confining surfaces is of critical significance [29–31]. Here, again, the interaction between the levitating body and its bounding elements is substantial.

Since the conduction of ground-effect experiments at rarefied-flow conditions is overwhelmingly costly, it is of evident interest to carry a theoretical study on the impact of ground surface on the aerodynamic properties of a moving vehicle. Apart from its practical significance, such analysis may shed light on possible fundamental differences between the impacts of ground proximity on the aerodynamic efficiency in continuum- and noncontinuum flow environments. In light of the above, and to extend the present state of knowledge, the current work investigates the aerodynamic properties and flow field over a flat plate set in the proximity of a planar boundary at large Knudsen numbers. Focusing on highly rarefied flow conditions, analytical and semianalytical predictions are obtained for the effect of the bounding surface in the free-molecular flow regime. A detailed study on the impact of the plate angle of attack, plate height, and surface conditions, is carried out. The effect of airfoil and ground reflections, varying between specular and diffuse emissions, is examined. The free-molecular results are validated through comparison with DSMC computations, to test the breakdown of the collisionless description with decreasing Knudsen numbers. The convergence of the results to the free-stream description is discussed, together with the qualitative differences from the counterpart ground effect problem at continuum conditions.

In Sec. II, the problem is stated. The free-molecular limit is analyzed in Sec. III, including both diffuse- and specular-wall solutions. The numerical DSMC scheme is described in Sec. IV, followed by our results and concluding comments in Secs. V and VI, respectively. Technical details are relegated to the Appendices.

II. STATEMENT OF THE PROBLEM

A Schematic of the problem is given in Fig. 1. Consider a stationary thin flat plate of length c^* placed in a two-dimensional stream of a monatomic hard-sphere gas of far-field density ρ_0^* , temperature T_0^* , and velocity $\mathbf{U}_0^* = U_0^* \hat{\mathbf{x}}$ (hereafter, asterisks denote dimensional quantities). The domain is confined by an x^* -directed (in the $\hat{\mathbf{x}}$ unit-vector direction) infinite planar surface. The plate midpoint, aligned with the axes origin, is placed at a distance H^* from the bounding plane and the plate surface is fixed at an angle of attack α to the x^* axis.

In the framework of gas kinetic theory and the steady two-dimensional setup considered, the gas state is governed by the velocity distribution function $f^* = f^*(\mathbf{r}^*, \boldsymbol{\xi}^*)$ of finding a gas molecule with position and velocity about $\mathbf{r}^* = (x^*, y^*)$ and $\boldsymbol{\xi}^* = (\xi_x^*, \xi_y^*, \xi_z^*)$, respectively. While the hydrodynamic (macroscopic) gas motion is confined to the (x, y) plane, molecular gas movements are

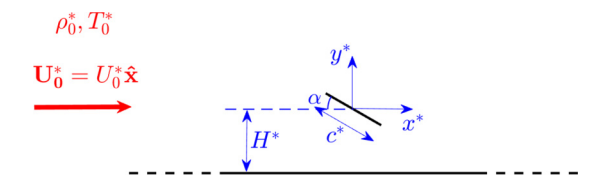


FIG. 1. Schematic of the problem: a thin flat plate of size c^* is set in a semi-infinite two-dimensional stream of far-field density ρ_0^* , temperature T_0^* , and velocity $\mathbf{U}_0^* = U_0^* \hat{\mathbf{x}}$ parallel to the ground. The plate midpoint (axes origin) is placed at a distance H^* from the ground and the plate surface is fixed at an angle of attack α in the clockwise direction to the negative x^* axis.

distributed in all spatial directions. We model gas-surface interactions of the gas particles with the plate and planar surface via the Maxwell boundary condition [32],

$$f(\mathbf{r}_{b}^{*}, \boldsymbol{\xi}^{*} \cdot \hat{\mathbf{n}} > 0) = \beta \frac{\rho_{b}^{*}(\mathbf{r}_{b}^{*})}{\pi^{3/2} U_{\text{mp}_{b}}^{*3}} \exp \left[-\frac{|\boldsymbol{\xi}^{*} - \mathbf{U}_{b}^{*}|^{2}}{U_{\text{mp}_{b}}^{*2}} \right] + (1 - \beta) f(\mathbf{r}_{b}^{*}, \boldsymbol{\xi}^{*} - 2(\boldsymbol{\xi}^{*} \cdot \hat{\mathbf{n}})\hat{\mathbf{n}}), \quad (1)$$

where the relative β and $(1-\beta)$ parts of the gas molecules are emitted diffusely and specularly, respectively, at each $\mathbf{r}_b^* = (x_b^*, y_b^*)$ location along the boundaries. Here, $\hat{\mathbf{n}}$ denotes a unit vector normal to the surface and into the gas, $\rho_b^*(\mathbf{r}_b^*)$ is a yet unknown function associated with the mass flux of particles emitted from the boundary, and $U_{\text{mp}_b}^* = \sqrt{2\mathcal{R}^*T_b^*}$ is the molecular most probable speed based on the boundary temperature T_b^* , with \mathcal{R}^* denoting the specific gas constant. The plate and planar boundaries are assumed isothermal and kept with the common far-stream temperature $T_b^* = T_0^*$. In line with the problem formulation for a stationary airfoil, it is assumed that the planar ground surface, as the far-field stream, acquires the velocity $\mathbf{U}_0^* = U_0^* \hat{\mathbf{x}}$. Thus, $\mathbf{U}_b^* = \mathbf{U}_0^*$ for the ground boundary, whereas $\mathbf{U}_b^* = \mathbf{0}$ for the plate. Clearly, the surface temperature and velocity are effective only for the diffusive (β -multiplied) part of the wall condition in Eq. (1), and do not impact the system response in cases where the boundaries are fully specular ($\beta = 0$).

In considering the Maxwell wall condition in Eq. (1), the fully diffuse β part represents a "rough scatterer," where the colliding particles attain thermal equilibrium with the interacting wall. The specular $1-\beta$ reflector then mimics a perfectly smooth wall. While none of these models exists in reality, it is commonly accepted that wall reflections from actual surfaces may be described, in a variety of applications, as their combination [32]. The Maxwell condition, commonly used in rarefied-gas-dynamics literature, has been chosen due to its simplicity and the ability to derive analytical solutions from it. It is clear that, by using a different scattering rule, the gas velocity and temperature at the wall would differ from those imposed by the present model, and the results should be quantitatively modified. This should be the case when imposing, for example, the Cercignani-Lampis interaction kernel [33], as suggested in several contexts. In the following, we prefer model simplicity over a more involved treatment of the boundary interaction, that may only quantitatively affect the results but obviate analysis.

To render the problem dimensionless, we scale the position by the plate length c^* , the velocity by $U^*_{\mathrm{mp}_0} = \sqrt{2\mathcal{R}^*T_0^*}$, and the density and temperature by ρ_0^* and T_0^* , respectively. The system scaled description is then governed by its reduced geometrical measures,

$$H = H^*/c^* \quad \text{and} \quad \alpha, \tag{2}$$

denoting the airfoil height and angle of attack, respectively, together with the normalized free-stream speed and chord-based mean Knudsen number

$$U_0 = U_0^* / U_{\text{mp}_0}^*$$
 and $\text{Kn} = \lambda^* / c^*$, (3)

respectively, and the surfaces accommodation coefficient β . In what follows, we study the steady flow field in a ground-affected stream at noncontinuum conditions, focusing on the limit of high

rarefaction rates. We start by analyzing the free-molecular $(Kn \to \infty)$ limit of the problem. No restrictions are made for the values of H, α , and U_0 , which allow the analysis of the aerodynamic problem at arbitrary heights, angles of attack, and far-stream velocities. The analysis is then complemented by numerical simulations of the problem at finite Knudsen numbers and comparison with existing results in the continuum limit.

III. FREE-MOLECULAR LIMIT

At free-molecular (Kn $\to \infty$) conditions, the velocity distribution function $f(\mathbf{r}, \boldsymbol{\xi})$ satisfies the collisionless two-dimensional (**r**-dependent) Boltzmann equation,

$$\xi_x \frac{\partial f}{\partial x} + \xi_y \frac{\partial f}{\partial y} = 0. \tag{4}$$

The equation is supplemented by the scaled form of the Maxwell boundary condition [cf. Eq. (1)],

$$f(\mathbf{r}_b, \boldsymbol{\xi} \cdot \hat{\mathbf{n}} > 0) = \beta \frac{\rho_b(\mathbf{r}_b)}{\pi^{3/2}} \exp[-|\boldsymbol{\xi} - \mathbf{U_b}|^2] + (1 - \beta)f(\mathbf{r}_b, \boldsymbol{\xi} - 2(\boldsymbol{\xi} \cdot \hat{\mathbf{n}})\hat{\mathbf{n}}), \tag{5}$$

assigned to the reflected particles at each solid surface. Here, $\mathbf{U_b} = \mathbf{U_0}$ over the planar ground and $\mathbf{U_b} = \mathbf{0}$ over the airfoil. At a given (x, y) location, particles that have not formerly interacted with any of the solid surfaces acquire the Maxwellian velocity distribution with the far-field flow properties,

$$f = f_{M_0} = \frac{1}{\pi^{3/2}} \exp\left[-\left((\xi_x - U_0)^2 + \xi_y^2 + \xi_z^2\right)\right]. \tag{6}$$

For particles that have interacted with a solid surface prior to reaching at a given location, the in-plane velocity vector (ξ_x, ξ_y) uniquely determines the identity of their recent emitting wall. The calculation of the probability density function then takes into account the respective wall conditions of the reflecting boundary. This is carried out in Secs. III A and III B, where the cases of fully diffuse $(\beta = 1)$ and fully specular $(\beta = 0)$ surfaces are analyzed separately, respectively. The combined diffuse-specular case is composed of the two limit cases examined and is therefore not discussed in detail hereafter.

A. Diffuse reflecting walls

Setting $\beta = 1$ in Eq. (5), the velocity distribution function of particles that have interacted with a solid surface is

$$f(\mathbf{r}, \boldsymbol{\xi}) = \frac{\rho_b(\mathbf{r_b})}{\pi^{3/2}} \exp[-|\boldsymbol{\xi} - \mathbf{U_b}|^2], \tag{7}$$

where $\rho_b(\mathbf{r_b})$ is an unknown function to be determined via imposition of the impermeability condition along each reflecting boundary. In Eq. (7), $\mathbf{r_b}$ is the point of particle recent wall reflection, specified by its present position \mathbf{r} and in-plane velocity vector (ξ_x, ξ_y). To formulate the no-penetration condition, we put

$$\int_{\boldsymbol{\xi}\cdot\hat{\mathbf{n}}>0} (\boldsymbol{\xi}\cdot\hat{\mathbf{n}}) f(\mathbf{r}_b,\boldsymbol{\xi}) d\boldsymbol{\xi} + \int_{\boldsymbol{\xi}\cdot\hat{\mathbf{n}}<0} (\boldsymbol{\xi}\cdot\hat{\mathbf{n}}) f(\mathbf{r}_b,\boldsymbol{\xi}) d\boldsymbol{\xi} = \rho(\mathbf{r}_b) \mathbf{U}_b \cdot \hat{\mathbf{n}}$$
(8)

along the planar ground and each side of the plate, where $\rho(\mathbf{r_b})$ denotes the gas density at $\mathbf{r} = \mathbf{r_b}$. Here, the first and second integrals express the contributions of outgoing and incoming particles to the macroscopic gas velocity normal to each surface, respectively. At a given location, approaching particles may arrive at the surface from other boundaries, yielding a coupled set of integral equations as detailed below. The right-hand side in Eq. (8) vanishes over the stationary plate wall, since $\mathbf{U_b} = \mathbf{0}$. Additionally, since $\mathbf{U_0}$ points in the x direction, $\mathbf{U_b} \cdot \hat{\mathbf{n}}$ vanishes at the ground y = -H surface as well.

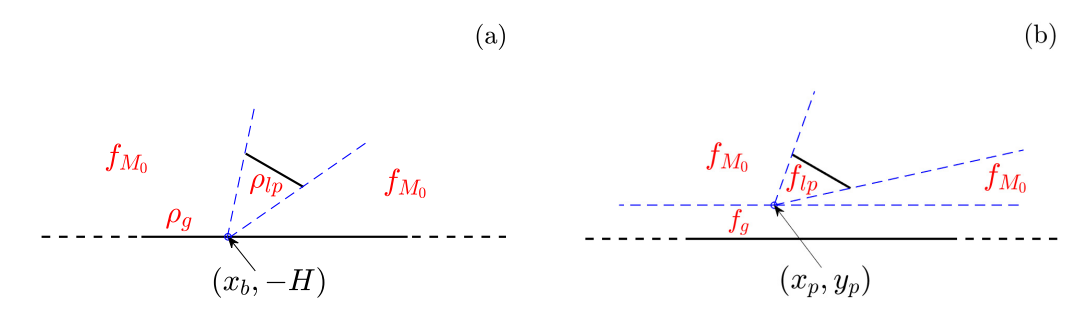


FIG. 2. Division of the free-molecular diffuse-wall flow domain for (a) the imposition of the impermeability condition at the point $(x_b, -H)$ along the y = -H wall and (b) the calculation of the hydrodynamic fields at the point (x_p, y_p) in the gas. The points $(x_b, -H)$ and (x_p, y_p) in (a) and (b) are marked by circles, respectively, and the dashed blue lines divide the flow field into separate regions of particles arriving from the different boundaries.

We detail the derivation of the walls impermeability condition at the ground y = -H surface. To this end, consider Fig. 2(a) and the imposition of the condition at the indicated $(x_b, -H)$ location. Applying Eq. (5) with $\beta = 1$, the contribution of the reflected particles integral in Eq. (8) is

$$\int_{\boldsymbol{\xi} \cdot \hat{\mathbf{n}} > 0} (\boldsymbol{\xi} \cdot \hat{\mathbf{n}}) f_g d\boldsymbol{\xi} = \frac{\rho_g(x_b)}{2\sqrt{\pi}},\tag{9}$$

where the subscript "g" denotes the ground-wall-associated function. To evaluate the in-flux integral contribution [second term on the right-hand side of Eq. (8)], we note that, at the indicated $(x_b, -H)$ location, particles may arrive from either the far field (distributed with f_{M_0}) or the lower plate surface (marked by "lp"), and no contribution arises from the "obscured" upper plate surface. This is illustrated in Fig. 2(a), where the dashed blue lines mark the separating ξ_x/ξ_y directions that divide between the different particles populations. Note that, at sufficiently large angles of attack α and x_b values (not illustrated here for brevity), the lower part of the plate becomes obscured and particles may reach the ground from the plate upper surface.

Considering the contribution of particles reflected from the lower plate surface, we obtain

$$\int_{\boldsymbol{\xi}\cdot\hat{\mathbf{n}}<0} (\boldsymbol{\xi}\cdot\hat{\mathbf{n}}) f_{lp} d\boldsymbol{\xi} = -\frac{1}{4\sqrt{\pi}} \int_{-1/2}^{1/2} \frac{\rho_{lp}(z)(z\sin\alpha - H)(x_b\sin\alpha - H\cos\alpha) dz}{\left[(z\sin\alpha - H)^2 + (x_b - z\cos\alpha)^2\right]^{3/2}},$$
 (10)

where z is a variable of integration along the plate lower surface. Expectedly, the integrand vanishes for $\alpha = \pi/2$ at $x_b = 0$. The contribution of far-field arriving particles, reaching the ground with no prior interaction with the solid boundaries, is divided into left-to-the-plate and right-to-the-plate portions. The former yields

$$\int_{\boldsymbol{\xi}\cdot\hat{\mathbf{n}}<0}^{(\text{left})} (\boldsymbol{\xi}\cdot\hat{\mathbf{n}}) f_{M_0} d\boldsymbol{\xi} = -\frac{1}{2\sqrt{\pi}} \left\{ \frac{\text{erf}(U_0) + 1}{2} + a \frac{\exp\left[\frac{a^2 U_0^2}{a^2 + 1} - U_0^2\right]}{2\sqrt{a^2 + 1}} \left[1 - \text{erf}\left(\frac{aU_0}{\sqrt{a^2 + 1}}\right) \right] \right\}, \quad (11)$$

whereas the latter is given by

$$\int_{\boldsymbol{\xi}\cdot\hat{\mathbf{n}}<0}^{(\text{right})} (\boldsymbol{\xi}\cdot\hat{\mathbf{n}}) f_{M_0} d\boldsymbol{\xi} = \frac{1}{2\sqrt{\pi}} \left\{ \frac{\text{erf}(U_0) - 1}{2} + b \frac{\exp\left[\frac{b^2 U_0^2}{b^2 + 1} - U_0^2\right]}{2\sqrt{b^2 + 1}} \left[1 - \text{erf}\left(\frac{bU_0}{\sqrt{b^2 + 1}}\right) \right] \right\}. \quad (12)$$

In Eqs. (11) and (12), "(left)" and "(right)" symbolically represent the left- and right-to-the airfoil limits of integration imposed by setup kinematics. Additionally, $\operatorname{erf}(s) = 2\pi^{-1/2} \int_0^s \mathrm{e}^{-t^2} \mathrm{d}t$ marks the Gauss error function and a and b follow from the limits of integration. In cases where $H \geqslant x_b \tan \alpha$, $a = -\frac{2x_b + \cos \alpha}{2H + \sin \alpha}$ and $b = -\frac{2x_b - \cos \alpha}{2H - \sin \alpha}$. If $b = -\frac{2x_b - \cos \alpha}{2H - \sin \alpha}$. If $b = -\frac{2x_b - \cos \alpha}{2H - \sin \alpha}$.

Substituting Eqs. (9)–(12) into Eq. (8), we obtain the impermeability condition at the point $(x_b, -H)$ depicted in Fig. 2(a), namely,

$$\begin{split} &2\rho_{g}(x_{b})-\int_{-1/2}^{1/2}\frac{\rho_{lp}(z)(z\,\sin\alpha-H)(x_{b}\sin\alpha-H\,\cos\alpha)\mathrm{d}z}{\left[(z\,\sin\alpha-H)^{2}+(x_{b}-z\,\cos\alpha)^{2}\right]^{3/2}}\\ &=2+a\frac{\exp\left[\frac{a^{2}U_{0}^{2}}{a^{2}+1}-U_{0}^{2}\right]}{\sqrt{a^{2}+1}}\left[1-\mathrm{erf}\left(\frac{aU_{0}}{\sqrt{a^{2}+1}}\right)\right]-b\frac{\exp\left[\frac{b^{2}U_{0}^{2}}{b^{2}+1}-U_{0}^{2}\right]}{\sqrt{b^{2}+1}}\left[1-\mathrm{erf}\left(\frac{bU_{0}}{\sqrt{b^{2}+1}}\right)\right]. \end{split} \tag{13}$$

Following similar arguments, the impermeability conditions over all other solid surfaces are derived and tabulated in Appendix A. These, together with the above Eq. (13), compose a system of coupled integral equations for the unknown flux functions, where the far-field stream particles contribute the nonhomogeneous forcing terms. In the case where U_0 vanishes, the expected uniform $\rho_g = \rho_{lp} = \rho_{up} = 1$ solution is captured. For any nonzero choice of U_0 , the impermeability conditions were solved numerically by discretizing the fluxes along the boundaries. To this end, the fluxes were represented by their discrete values at points along the walls, with the integral terms evaluated using the trapezoidal rule. This resulted in a system of linear coupled nonhomogeneous algebraic equations that was inverted using a MATLAB subroutine. Converged results were obtained with a scaled discretization step of $\approx 10^{-3}$ along the solid surfaces, constituting a minor computational effort compared with the numerical DSMC calculations described below.

Having determined the walls fluxes, the velocity distribution function in Eq. (7) is known, and the hydrodynamic fields may be computed via appropriated quadratures over the velocity space. Specifically, the density ρ , and x- and y-velocity components, u_x and u_y , are given by

$$\rho(x,y) = \int_{-\infty}^{\infty} f \, d\boldsymbol{\xi}, \quad u_x(x,y) = \frac{1}{\rho(x,y)} \int_{-\infty}^{\infty} \xi_x f \, d\boldsymbol{\xi}, \quad \text{and} \quad u_y(x,y) = \frac{1}{\rho(x,y)} \int_{-\infty}^{\infty} \xi_y f \, d\boldsymbol{\xi},$$
(14)

respectively, whereas the normal $(P_{xx}, P_{yy}, \text{ and } P_{zz})$ and shear (P_{xy}) stresses are computed via

$$P_{xx}(x,y) = \int_{-\infty}^{\infty} (\xi_x - u_x)^2 f \, d\xi, \quad P_{yy}(x,y) = \int_{-\infty}^{\infty} (\xi_y - u_y)^2 f \, d\xi,$$

$$P_{zz}(x,y) = \int_{-\infty}^{\infty} \xi_z^2 f \, d\xi, \quad \text{and} \quad P_{xy}(x,y) = \int_{-\infty}^{\infty} (\xi_x - u_x)(\xi_y - u_y) f \, d\xi,$$
(15)

respectively. The pressure field is obtained by superposing

$$p(x, y) = \frac{2}{3}(P_{xx} + P_{yy} + P_{zz}),$$

and the temperature $T=p/\rho$, in accordance with the scaled ideal-gas equation of state. At each (x,y) location, the above integrations average the contributions of particles arriving from the various boundaries, in accordance with the setup geometry. Similarly to the calculation of the boundary fluxes, particles may arrive at a given position from only part of the boundaries, while others are obscured. This is illustrated in Fig. 2(b), where the flow field is divided into four sections of particles arriving at the indicated (x_p, y_p) point from the far-field, ground wall, and lower surface of the airfoil. The integrations specified in Eqs. (14) and (15) are carried out in accordance with the geometrical restrictions at each location, to yield the desired (x,y) distributions of the hydrodynamic fields in the entire flow field.

B. Specular reflecting walls

Taking $\beta = 0$ in Eq. (5), the macroscopic impermeability condition is identically satisfied at a specular surface, where the particles undergo mirrorlike reflections with the value of the velocity

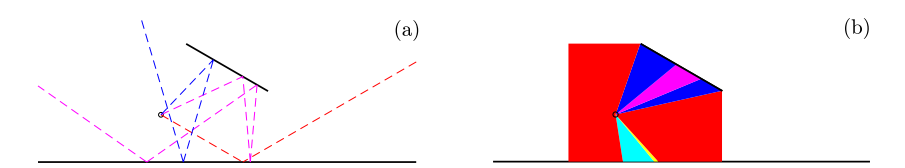


FIG. 3. Free-molecular particle kinematics in a specular-wall system with H=1 and $\alpha=\pi/6$. (a) Trajectories of particles arriving at (x,y)=(-0.7,-0.5) (marked by a circle) after a single collision with the ground wall (dashed red line); one collision with the ground and then with the plate (dashed blue curve); and two collisions with each of the walls, starting with the ground (dashed magenta line). (b) Division of the flow field into sections of particles arriving at (x,y)=(-0.7,-0.5) following distinct sequences of collisions with the confining walls: the red sectors mark directions of particles colliding once with the ground or arrive directly at the point; the blue sectors depict particles that collide first with the ground and then with the plate; the cyan sector indicates particles that collide once with the plate in between two collisions with the ground; the magenta sector confines particles reaching (-0.7, -0.5) after colliding twice with each surface, starting with the ground; and the thin yellow sector denotes particles that similarly interact twice with each wall, yet start with the airfoil.

distribution function preserved. Generally, a particle passing through the domain confined between the ground and lower plate surface may undergo several collisions with the bounding walls. The sequence of collisions, determining the particle trajectory, depends on problem geometrical parameters H and α and the particle in-plane velocity direction at entering the domain. This is illustrated in Fig. 3, where the free-molecular trajectories in a specular-wall system with H=1 and $\alpha=\pi/6$ are presented. Figure 3(a) shows three examples for particle trajectories arriving at (x,y)=(-0.7,-0.5) after distinct sets of wall collisions. Figure 3(b) then divides the flow field into sections of particles arriving at (x,y)=(-0.7,-0.5) after different sequences of surface collisions. Particles approaching the plate at distances higher than $H+0.5 \sin \alpha$ from the ground (i.e., with $y>0.5 \sin \alpha$) may experience only one collision with the upper plate surface, and their trajectories are simple to follow.

Focusing on the confined plate-ground domain $[x \in (-0.5 \cos \alpha, 0.5 \cos \alpha)]$ with $y \in (-H, 0.5 \sin \alpha)]$, where the ground effect is most dominant, we first note that particles colliding with the horizontal ground surface restore their value of f with their ξ_y sign flipped. In difference, a particle interacting with the lower plate surface inclined at an angle α changes its in-plane velocity with a 2α rotation relative to the plate normal direction. More specifically, after its first collision with the plate lower side, the particle velocity distribution function changes from Eq. (6) to

$$f_{(1,0)} = \frac{1}{\pi^{3/2}} \exp\left[-(\xi_x - U_0 \cos 2\alpha)^2 - (\xi_y + U_0 \sin 2\alpha)^2 - \xi_z^2\right],\tag{16}$$

to maintain its precollision value. Here, the subscript (l,q) marks the number of times that the particle has collided with the plate (l) and ground (q) walls. If the above particle then collides with the ground wall, its postcollision distribution becomes

$$f_{(1,1)} = \frac{1}{\pi^{3/2}} \exp\left[-(\xi_x - U_0 \cos 2\alpha)^2 - (\xi_y - U_0 \sin 2\alpha)^2 - \xi_z^2\right],\tag{17}$$

in line with the change in sign in ξ_y . Following similar arguments, a particle undergoing a sequence of l collisions with the lower plate, intervened by q interactions with the ground wall, obtains the velocity distribution function

$$f_{(l,q)} = \frac{1}{\pi^{3/2}} \exp\left[-(\xi_x - U_0 \cos 2l\alpha)^2 - [\xi_y + (-1)^{l+q-1} U_0 \sin 2l\alpha]^2 - \xi_z^2\right].$$
 (18)

To obtain the specular-wall system response, the above calculation should be repeated for all in-plane particle directions at each (x, y) location of interest, yielding $f(x, y, \xi)$ in the

five-dimensional phase space. The sorting procedure at a given position is illustrated in Fig. 3(b) at (x, y) = (-0.7, -0.5) for a system with H = 1 and $\alpha = \pi/6$, as in Fig. 3(a). Once the velocity distribution function is known, the hydrodynamic fields are computed via the quadratures specified in Eqs. (14) and (15).

IV. NUMERICAL SCHEME: DSMC METHOD

The DSMC method is the prevalent scheme for simulating noncontinuum gas flows [34]. The method was initially applied as a direct numerical approach for calculating dilute gas dynamics, and was later on shown to yield results that converge to the solution of the Boltzmann equation [35]. Within the computational framework, the velocity distribution function of the gas molecules is represented by a number of computational particles. The domain is divided into a mesh of cells whose size Δs^* is smaller than the particles mean free path λ^* . The particles motions and interactions are decoupled over a time step Δt^* , being shorter than the local mean free time τ^* between collisions. At each time step, the particles are first translated following "free-flight" kinematics, as if they do not interact with each other. Then, the particles are sorted into computational cells and collisions are evaluated stochastically, conserving the collision momentum and energy invariants. The computational cells are used for evaluating the macroscopic fields, which are obtained through weighted averages of the particles' properties.

We applied the DSMC algorithm to analyze the ground effect problem for arbitrary, and in particular large, Knudsen numbers. The calculation serves as a means for supporting our analytical free-molecular solution and describing its breakdown with decreasing Kn. To this end, the interaction between the gas molecules was calculated based on the commonly used hard-sphere model of molecular interaction. This choice was motivated by its simple implementation in calculations. The impact of molecular collisions different from hard spheres, not considered hereafter, is expected to affect the results only quantitatively, and should not change the qualitative nature of our findings. The two-dimensional computational domain was divided into cells of equal size not exceeding $\Delta x^* = 0.05\lambda^*$, and the time step was set no larger than $\Delta t^* = 0.01\tau^*$. To simulate a finite gas volume, artificial side and top bounding surfaces were added at $x = \pm 7$ and y = 7, respectively, over which open boundary conditions were imposed. Gas particles leaving the simulation domain through the open surfaces were deleted from the calculation, while entering particles were acquired by the free-stream Maxwellian distribution. We have validated that the added edges were located far enough so as to not affect our numerical results for the near-field ground effect. At the initial state, the simulation domain contained no particles. Then, at each time step, computational particles were allowed to enter through the added boundaries, by sampling the flux of the Maxwellian distribution in Eq. (6). Particles crossing these boundaries from inside the domain were removed from the simulation, and diffuse or specular reflections were applied to model the scattering from the ground and plate solid walls. The simulation was followed until a steady state was formed, by letting the transient behavior evolve into a time-independent solution. The calculation of macroscopic quantities commenced after a steady state was achieved, with the sampling time duration determined by requiring that the relative statistical error does not exceed $\approx 5\%$ of the signal. A typical calculation was carried out using a computational grid of \approx 280 cells in the x direction and \approx 160 cells in the y direction, for a domain of scaled x-size = 14 and y-size = 7 + H in plate-length units. Taking \approx 200 particles per cell, a sample of \approx 9 × 10⁶ particles was considered. Each computation lasted several hours using an Intel[®] CoreTM i7-11800 machine (24M Cache, up to 4.60 GHz). To verify the accuracy of results, a convergence analysis (not detailed here for brevity) was carried out. This has indicated that our simulation predictions are nearly unaffected by a further decrease in the above-mentioned cells size and time step, or by an increase in the number of particles taken per cell, ensuring the grid independence of our DSMC predictions.

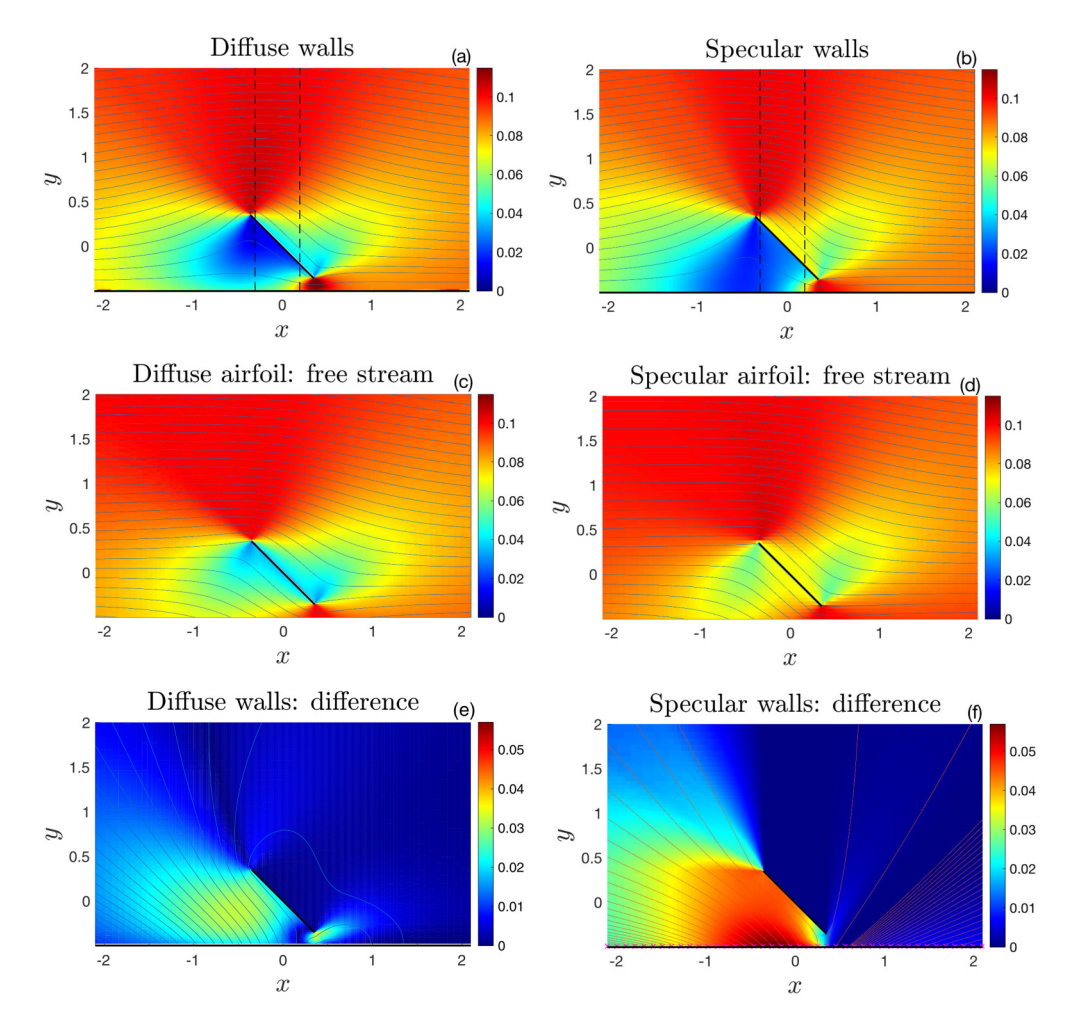


FIG. 4. Colormaps of the free-molecular velocity magnitude about an airfoil set at H=0.5, $\alpha=\pi/4$, and $U_0=0.1$ in diffuse- (a), (c), (e) and specular- (b), (d), (f) wall systems. (a) and (b) present results for the full plate-ground problem; (c) and (d) show the counterpart free-stream fields (in the absence of ground); and (e) and (f) depict the difference between the full and free-stream fields. The thin curves show the respective flow streamlines. The dashed vertical lines in (a) and (b) mark the sections along which the results in Fig. 6 are presented.

V. RESULTS AND DISCUSSION

While the scheme of solution is valid for arbitrary values of the incoming flow velocity, ground-effect applications commonly require the velocity magnitude to be small. In the following we therefore fix $U_0 = 0.1$ to present most of our results. Additionally, we primarily consider a case where $\alpha = \pi/4$ and take H = 0.5, to focus on a configuration where the plate-ground interaction is expected to be strong.

Figure 4 presents the free-molecular velocity flow field at the above parameters combination. To this end, Figs. 4(a) and 4(b) show the velocity magnitude colormaps and streamlines for diffuse and specular-wall systems, respectively. For comparison, Figs. 4(c) and 4(d) present the counterpart "free-stream" results (i.e., in the absence of the ground). Figures 4(e) and 4(f) then depict the magnitudes and streamlines of the vector fields obtained by the difference between the above full and free-stream calculations.

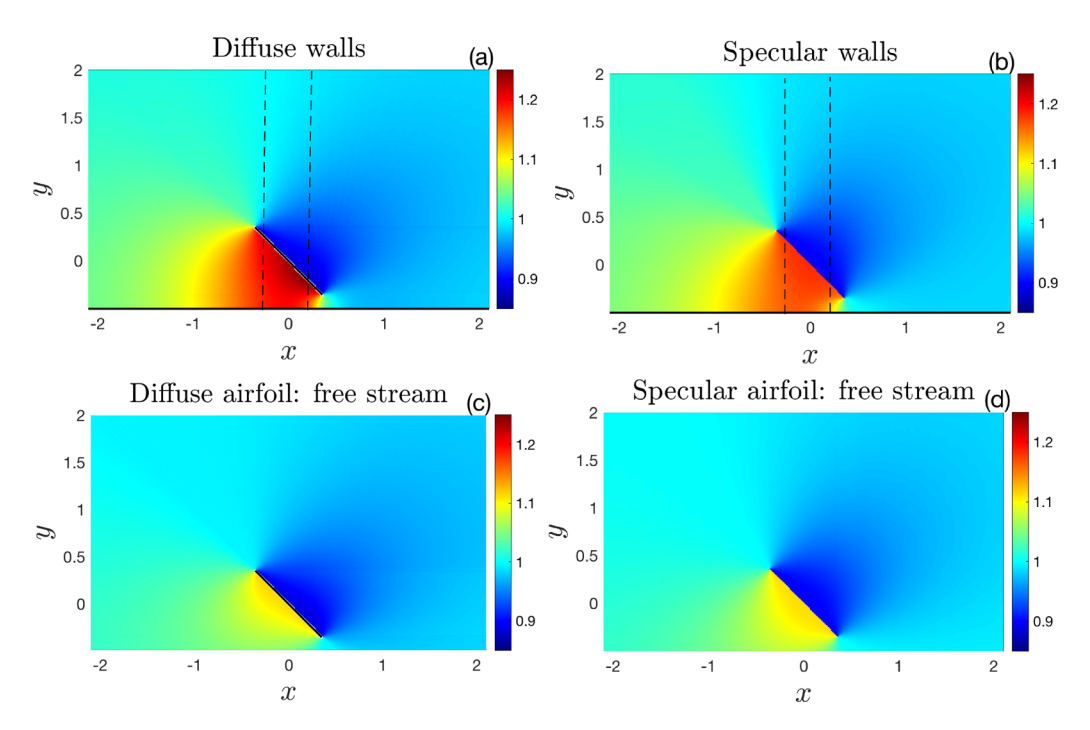


FIG. 5. Colormaps of the free-molecular pressure about an airfoil set at H=0.5, $\alpha=\pi/4$, and $U_0=0.1$ in diffuse- (a), (c) and specular- (b), (d) wall systems. (a) and (b) present results for the full plate-ground problem, and (c) and (d) show the counterpart free-stream fields (in the absence of ground). The dashed vertical lines in (a) and (b) mark the sections along which the results in Figs. 6(b) and 6(d) are presented.

Starting with the previously analyzed free-stream field [11,12], we observe that the solution in Figs. 4(c) and 4(d) is expectedly antisymmetric about the plate midchord axis. Higher slip magnitudes and velocity gradients over the plate are detected in Fig. 4(d) compared with Fig. 4(c), in line with the difference between specular and diffuse wall conditions. The symmetry inevitably breaks down in the presence of the ground, as shown in Figs. 4(a) and 4(b). Specifically, while the flow above the plate remains nearly unchanged, the strong interaction between the plate lower surface and the ground boundary yields a zone of significantly low speeds. Additionally, the velocity streamlines are deflected in the ground vicinity to satisfy impermeability. The net ground effect is depicted in Figs. 4(e) and 4(f), showing the difference between the vector flow fields with and without the ground surface, obtained by the vector difference between the results in Figs. 4(a) and 4(b) and Figs. 4(c) and 4(d), respectively. Here, a stagnant zone is observed above the plate, where ground reflections only weakly reach at free-molecular conditions. As in Figs. 4(c) and 4(d), significantly higher flow gradients are visible in the specular-system setup. The vector field "streamlines" in Figs. 4(e) and 4(f) mark the separate contribution of ground reflections (and repeated ground-plate interactions) to the total flow field, indicating the emission of gas particles away from the ground and parallel to the plate lower side.

To complement Fig. 4, Fig. 5 shows, at the same parameter combination of H = 0.5, $\alpha = \pi/4$, and $U_0 = 0.1$, colormaps of the free-molecular pressure field in diffuse- and specular-wall systems. In each setup, the full plate-ground and free-stream solutions are compared, illustrating, as in Fig. 4, the strong ground impact in the vicinity of the lower airfoil surface. The effect is qualitatively similar in both diffuse- and specular-wall systems, marking a zone of high pressure between the airfoil and the ground. This reflects the molecular interaction between the solid surfaces analyzed in Sec. III, and accompanied by the vanishing macroscopic flow speeds, presented in Figs. 4(a) and 4(b).

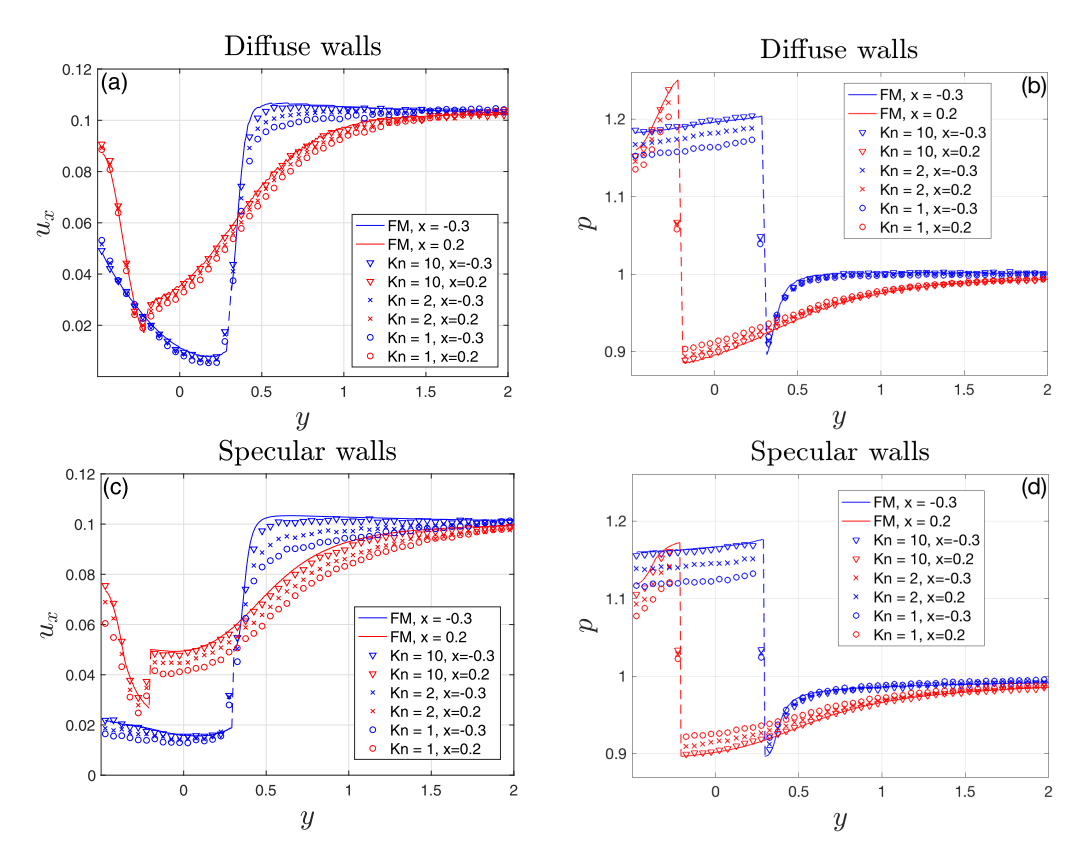


FIG. 6. Comparison between free-molecular (marked FM, in solid lines) and DSMC (symbols) predictions for the x velocity (a),(c) and pressure (b),(d) fields along x = -0.3 (in blue) and x = 0.2 (in red). (a) and (b) show results for the diffuse-wall system and (c) and (d) present data for the specular-wall problem. The triangles, crosses, and circles show DSMC data at Kn = 10, 2, and 1, respectively. All results are for an airfoil set at $\alpha = \pi/4$ with $U_0 = 0.1$. The dashed lines connect free-molecular data points between opposite sides of the airfoil.

To validate the free-molecular solution and examine its breakdown with decreasing rarefaction, Fig. 6 presents a comparison of the collisionless flow field with DSMC calculations at finite Knudsen numbers. The figure shows the y variations of the x velocity and pressure fields along the x = -0.3 and x = 0.2 sections, marked in Figs. 4(a), 4(b), 5(a), and 5(b) by the vertical dashed lines, in both diffuse- and specular-wall systems. Following the results in Figs. 4 and 5, steep gradients are observed in all cases in the vicinity of the plate surface, accompanied by field discontinuities between the plate upper and lower sides. The convergence of the Kn = 10 DSMC results to the free-molecular predictions is clearly observed. The collisionless description becomes less effective with decreasing Kn, yet remains within $\lesssim 5\%$ difference from DSMC data through Kn $\gtrsim 1$.

We next examine the ground effect on the aerodynamic force imposed on the plate. The force components are calculated via integration of the normal and shear stresses over the airfoil surface. Using $\rho_0^* U_{\rm mp_0}^{*2} c^*$ for scaling, the y-directed plate lift force per unit span is given by

$$L = \int_{-0.5}^{0.5} [(P_{\tilde{y}\tilde{y}}(\tilde{x}, \tilde{y} = 0^{-})\cos\alpha - P_{\tilde{x}\tilde{y}}(\tilde{x}, \tilde{y} = 0^{-})\sin\alpha) - (P_{\tilde{y}\tilde{y}}(\tilde{x}, \tilde{y} = 0^{+})\cos\alpha - P_{\tilde{x}\tilde{y}}(\tilde{x}, \tilde{y} = 0^{+})\sin\alpha)]d\tilde{x},$$
(19)

where (\tilde{x}, \tilde{y}) denote a system of coordinates originating at the plate midchord and directed in parallel $(\tilde{x}$ -wise) and normal $(\tilde{y}$ -wise) to the airfoil. The stress components appearing in Eq. (19) are the normal $(P_{\tilde{y}\tilde{y}})$ and shear $(P_{\tilde{x}\tilde{y}})$ stresses, calculated using Eq. (15) and projecting the x and y directions onto \tilde{x} and \tilde{y} , respectively. Similarly, the x-directed scaled drag force per unit span is calculated via

$$D = \int_{-0.5}^{0.5} [(P_{\tilde{y}\tilde{y}}(\tilde{x}, \tilde{y} = 0^{-}) \sin \alpha + P_{\tilde{x}\tilde{y}}(\tilde{x}, \tilde{y} = 0^{-}) \cos \alpha) - (P_{\tilde{y}\tilde{y}}(\tilde{x}, \tilde{y} = 0^{+}) \sin \alpha + P_{\tilde{x}\tilde{y}}(\tilde{x}, \tilde{y} = 0^{+}) \cos \alpha)] d\tilde{x},$$

$$(20)$$

and the impact of problem parameters on L and D is examined below. To this end, we recapitulate the counterpart expressions for the free-molecular aerodynamic forces on an inclined plate in a nonconfined setup [11,12]. Considering a diffuse-reflecting plate, the collisionless free-stream (FS) forces normal (F_N) and parallel (F_S) to the plate are

$$F_N^{\text{(FS,diff)}} = \frac{1}{2} \left[(2U_N^2 + 1) \text{erf}(U_N) + \frac{2}{\sqrt{\pi}} U_N \exp\left[-U_N^2 \right] + \sqrt{\pi} U_N \right]$$
 (21)

and

$$F_S^{(\text{FS,diff})} = U_S \left[U_N \operatorname{erf}(U_N) + \frac{1}{\sqrt{\pi}} \exp[-U_N^2] \right], \tag{22}$$

respectively, whereas for a specular plate

$$F_N^{(\text{FS,spec})} = (2U_N^2 + 1)\text{erf}(U_N) + \frac{2}{\sqrt{\pi}}U_N \exp\left[-U_N^2\right]$$
 (23)

and $F_S^{(\text{FS},\text{spec})} \equiv 0$. In Eqs. (21)–(23), $U_N = U_0 \sin \alpha$ and $U_S = U_0 \cos \alpha$. In terms of F_N and F_S , the lift and drag forces are

$$L = F_N \cos \alpha - F_S \sin \alpha \quad \text{and} \quad D = F_N \sin \alpha + F_S \cos \alpha, \tag{24}$$

respectively.

Figure 7 presents the variations of the lift and drag forces with the plate π -scaled angle of attack. Following Figs. 4–6, an airfoil of midchord height H=0.5 above the ground is considered. Two values of the incoming flow speed are inspected, namely, $U_0=0.1$ and $U_0=0.2$. The solid lines show the full free-molecular results, and the dashed curves depict the counterpart free-stream variations based on Eqs. (21)–(23). In the specular-wall case in Figs. 7(c) and 7(d), the dash-dotted lines show the approximate results derived in Appendix B. The triangles, crosses, and circles in all figure parts mark DSMC data at Kn = 10, 2, and 1, respectively.

At first we note that the free-molecular loading at ground effect is invariably larger than its nonconfined counterpart, for both lift and drag. This manifests the general impact of the ground surface as a "reflecting source" for particles originating at the free stream and reversing their y-velocity direction upon interacting with the airfoil. As in the nonconfined problem, the lift varies nonmonotonically with $0 \le \alpha \le \pi/2$ and the drag is monotonically increasing. Yet, while the maximum lift is obtained at $\alpha = \pi/4$ in the nonconfined problem, ground reflections shift its location to lower values, particularly in the specular-wall setup [cf. the solid lines in Figs. 7(a) and 7(c)]. This is attributed to the increased number of particles reaching the plate lower surface after multiple ground emissions for $\alpha < \pi/4$, resulting from the combined (and asymmetric) influences of airfoil inclination and positive-x-directed far-field stream. Different from the specular-wall case, we note that the diffuse-wall lift force does not vanish at the plate horizontal ($\alpha = 0$) and vertical $(\alpha = \pi/2)$ system configurations, but assumes a finite positive value. This, again, is an outcome of the ground effect, combined with the irreversibility of the diffuse-wall condition. Specifically, contributed by the distributions of P_{vv} (at $\alpha = 0$) and P_{xv} (at $\alpha = \pi/2$) along the airfoil surface [see Eq. (19)], it is the asymmetry caused by ground reflections, combined with the preferred direction of free-stream velocity, that yield a nonvanishing lift value. This asymmetry is not observed in the

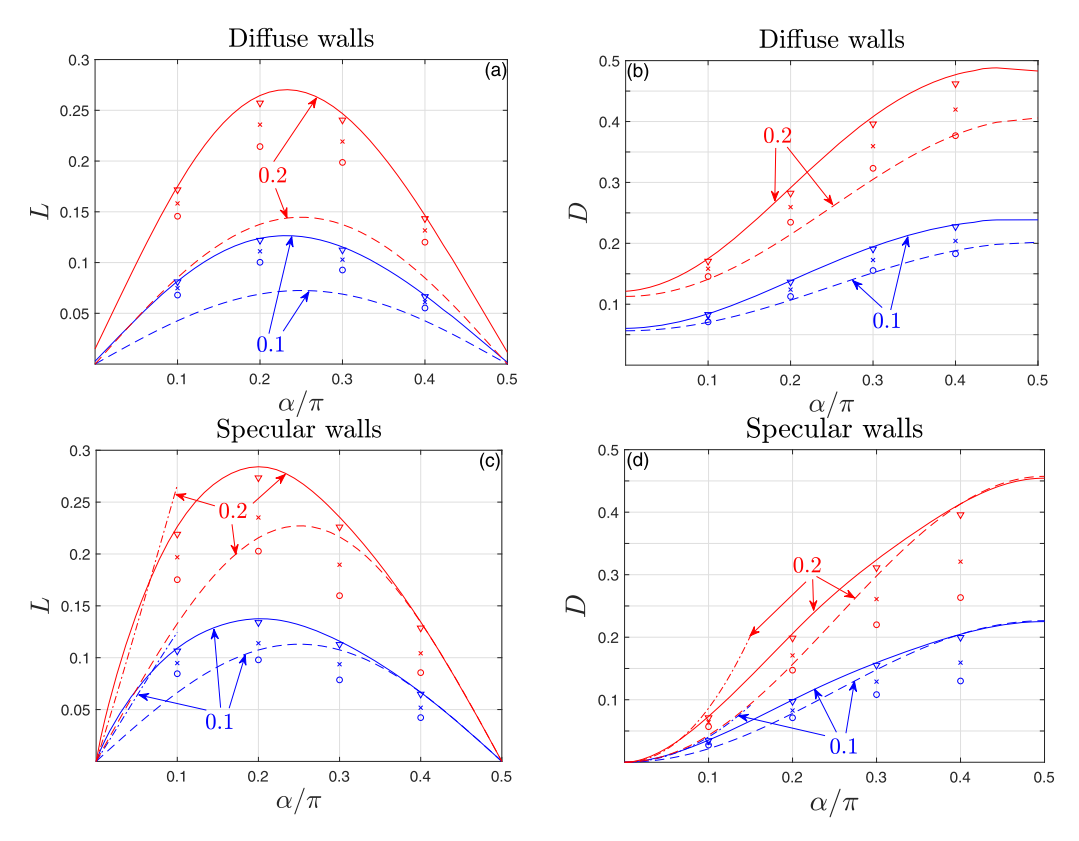


FIG. 7. Variations of the (a),(c) lift and (b),(d) drag forces with the plate scaled angle of attack α/π for diffuse- (a),(b) and specular- (c),(d) wall systems at the indicated values of $U_0 = 0.1$ (in blue) and $U_0 = 0.2$ (in red). The solid lines show ground-effect free-molecular results with H = 0.5, and the dashed curves present counterpart free-stream data. The triangles, crosses, and circles mark DSMC data at Kn = 10, 2, and 1, respectively. The dash-dotted lines in (c) and (d) depict the $\alpha \ll 1$ approximation derived in Appendix B.

specular case (where the lift vanishes at both $\alpha = 0$ and $\pi/2$), due to the symmetric form of the boundary condition.

Expectedly, an increase in the far-field flow speed magnifies the free-molecular forcing on the plate (cf. the blue and red curves in all parts of Fig. 7). Here, in common to both confined and nonconfined configurations, the loading scales linearly with U_0 , yielding the doubling of the lift and the drag components as the incoming speed is increased from $U_0 = 0.1$ to $U_0 = 0.2$. Comparing between DSMC and free-molecular results, we observe that all simulation predictions converge to their collisionless limit with increasing Kn, exhibiting deviations that are $\leq 3\%$ (and, in most cases, considerably lower) at Kn = 10. Additionally, satisfactory agreement is observed between the specular-wall free-molecular (solid curves) and approximate (dash-dotted lines) results in Figs. 7(c) and 7(d) at $\alpha \ll 1$. Here, the visible discrepancies are attributed to the nonlarge H = 0.5 value considered, whereas the approximate analysis strictly holds at $H \gg 1$.

The effect of plate height above the ground on the free-molecular lift force is examined in Fig. 8, showing, for diffuse- and specular-wall systems at $U_0 = 0.2$, the convergence of the α lift variation with increasing H to the free-stream solution. At each angle of attack, an increase in the plate-ground distance reduces the lift magnitude, which uniformly approaches its free-stream value, marked by the dashed blue curves. For H < 0.5 plate-ground distances, the lift curve is plotted for only part

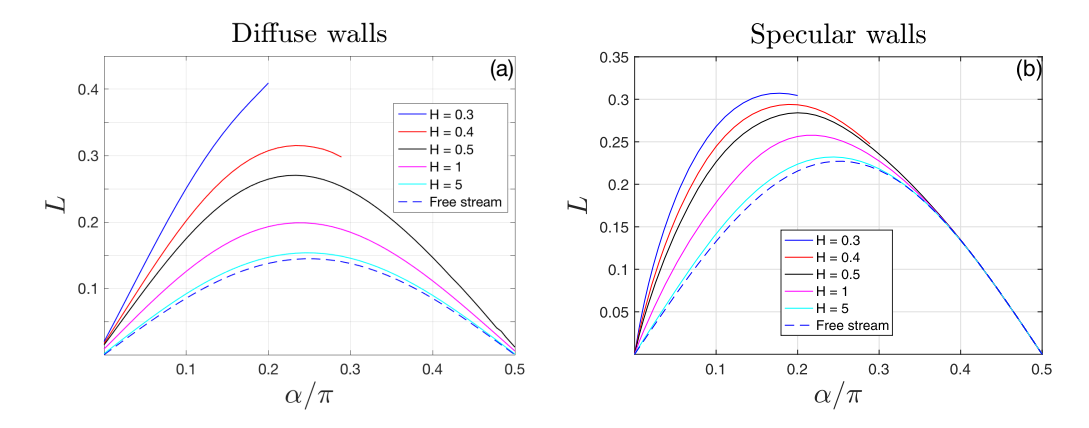


FIG. 8. Convergence of the free-molecular lift force to its free-stream value with increasing plate-ground distance: variations of L with α/π at $U_0=0.2$ and the indicated values of H in diffuse- [Fig. 9(a)] and specular- [Fig. 9(b)] wall setups. The dashed blue line in each figure part presents the respective free-stream variations.

of the $\alpha \in [0, \pi/2]$ interval, namely, $\alpha \in [0, \sin^{-1}(2H)]$, due to the kinematic restriction on plateground separation.

We conclude the discussion of results by comparing our high-Kn flow calculations with existing continuum-limit (Kn \ll 1) results. To this end, we consider the ideal-flow (Kn \rightarrow 0) incompressible flow regime, for which the two-dimensional drag force vanishes, and the lift loading was previously computed and tabulated [4]. To make the comparison transparent, we inspect the deviation of the force from its free-stream counterpart, and scale the difference by the free-stream value. Consequently, the common difference in scaling between the two limits is avoided. To recall, the dimensional ideal-flow lift over an $\alpha \ll 1$ inclined flat plate set at a low-speed (incompressible) flow field is [36]

$$L^{*(\text{FS})}(\text{Kn} \to 0) = \pi \, \rho_0^* U_0^{*2} c^* \alpha.$$

In the following we compare between the values of $(L-L^{\rm (FS)})/L^{\rm (FS)}$ obtained in the highly rarefied and ideal flow limits.

Figure 9 presents the variations of the scaled lift force, $(L-L^{(FS)})/L^{(FS)}$, with the plate midchord height H, in the free-molecular and ideal-flow incompressible limits. Small values for the plate angle of attack, $\alpha = \pi/36$ [in Fig. 9(a)] and $\alpha = \pi/18$ [in Fig. 9(b)], are taken, so that the ideal-flow analysis holds. For these values, the black curves depict the $Kn \to 0$ incompressible-flow results tabulated in Ref. [4]. These results should be valid for all $U_0 \ll 1$, as long as incompressible-flow conditions prevail. Additionally, the solid blue and red curves show the counterpart free-molecular distributions for specular- and diffuse-wall systems at $U_0 = 0.1$, respectively, and the dashed lines present the corresponding specular-wall approximation derived in Appendix B.

Inspecting Fig. 9, we note that the relative lift deviations are considerably larger in the free-molecular limit compared with the ideal-flow limit. Indeed, in the absence of molecular collisions it is expected that the effect of ground reflections is communicated more efficiently to the airfoil, undisturbed by intermolecular interactions. In line with the results in Figs. 7 and 8, the ground increases the airfoil lift compared with its free-stream value for all H. This is markedly different from the continuum-limit predictions, indicating a slight decrease in lift (i.e., negative $L - L^{(FS)}$) for $H \gtrsim 1.3$ at $\alpha = \pi/36$ and $H \gtrsim 0.7$ at $\alpha = \pi/18$. At the small angles of attack considered, we observe only small differences between the diffuse- and specular-wall systems. Additionally, the free-molecular results are relatively well captured by the specular-wall approximation (marked by the dashed blue line) at large enough $H \gtrsim 1$. The ground-induced lift deviation vanishes at $H \gg 1$

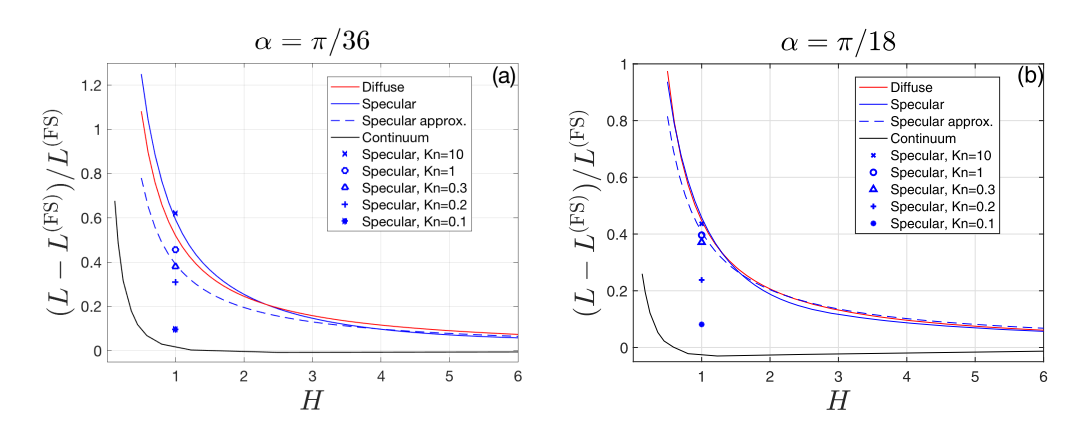


FIG. 9. Comparison between the H variations of the free-molecular and ideal-flow scaled lift forces, $(L - L^{(FS)})/L^{(FS)}$, over an airfoil set at $\alpha = \pi/36$ (a) and $\alpha = \pi/18$ (b). In each part, the solid blue and red curves show the free-molecular results in specular- and diffuse-wall systems at $U_0 = 0.1$, respectively, and the dashed line presents the counterpart specular-wall approximation derived in Appendix B. The black curves depict the ideal (Kn \rightarrow 0) incompressible-flow variation calculated in Ref. [4]. The symbols indicate the scaled lift forces, obtained via DSMC calculations, at the indicated Knudsen numbers in a specular-wall system.

in all cases. Specifically, our calculations indicate that the free-molecular plate forcing coincides with its free-stream value [stated in Eqs. (21)–(23)] for $H \geq 9$.

The effect of gas rarefaction on the scaled lift force is depicted in both parts of Fig. 9 by DSMC predictions, calculated at H=1 and marked by symbols for a specular-wall system. The results illustrate the impact of decreasing rarefaction in reducing the scaled lift, indicating that the main transition occurs at intermediate $0.1 \le \text{Kn} \le 1$ Knudsen numbers. Rigorous rationalization of the passage between the free-molecular and continuum limits, that should be based on analysis of the kinetic model and incorporate the effect of molecular collisions, is deferred to future inspection.

VI. CONCLUSION

We investigated the impact of gas rarefaction on the two-dimensional aerodynamic ground effect over a flat plate. Focusing on highly rarefied flow conditions, we formulated the free-molecular problem based on the collisionless Boltzmann equation and the Maxwell boundary conditions. A semianalytical solution was derived, where specular and diffuse surface reflections were studied separately. The calculated ballistic field was compared with direct simulation Monte Carlo computations at finite Knudsen numbers to test its validity and breakdown with decreasing rarefaction. The specific effect of ground reflections was illustrated through comparison with the nonconfined (plate in a "free stream") flow field. The results indicate that the ground invariably increases the aerodynamic loading on the plate and shifts the maximum lift value to lower angles of attack compared with the nonconfined configuration. While the ground may yield a negative contribution to the lift in the continuum (ideal-flow) limit, its relative difference compared with the nonconfined setup is found significantly larger and consistently positive at highly rarefied conditions.

Recalling continuum aerodynamics literature, the ground effect is commonly considered in the context of a three-dimensional setup, to examine its impact on induced drag loading over a finite wing [36]. A desirable extension of the present work would therefore be a counterpart investigation on the effect of ground confinement at noncontinuum conditions. Such analysis, that should be preceded by a study on rarefied-gas aerodynamics over a finite wing in free stream, constitutes a topic for future work.

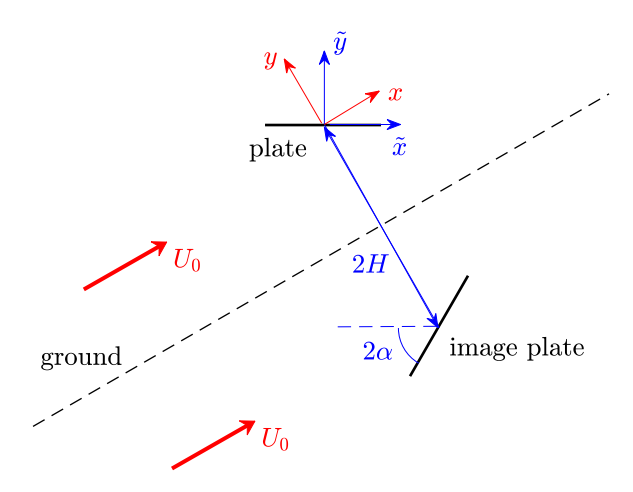


FIG. 10. Schematic of the two-plate system equivalent to the specular-wall ground configuration.

ACKNOWLEDGMENT

This research was supported by the Israel Science Foundation (Grant No. 163/25).

DATA AVAILABILITY

The data supporting this study's findings are available within the article.

APPENDIX A: IMPERMEABILITY CONDITIONS IN A DIFFUSE-WALL SETUP

Following similar considerations to those described in Sec. III A, the impermeability conditions over the airfoil lower and upper surfaces are derived. Skipping the technical details of calculation, the condition over the lower airfoil side is given by

$$2\rho_{\rm lp}(x_b) - \int_{-\infty}^{H/\tan\alpha} \frac{\rho_g(z)(H - x_b \sin\alpha)(H \cos\alpha - z \sin\alpha)dz}{[(H - x_b \sin\alpha)^2 + (x_b \cos\alpha - z)^2]^{3/2}}$$

$$= 2\int_0^\infty z[\text{erf}(U_0 \cos\alpha - z \cot\alpha) + 1] \exp[-(z - U_0 \sin\alpha)^2]dz, \tag{A1}$$

whereas along its upper side

$$2\rho_{\rm up}(x_b) - \int_{H/\tan\alpha}^{\infty} \frac{\rho_g(z)(H - x_b \sin\alpha)(H \cos\alpha - z \sin\alpha)dz}{[(H - x_b \sin\alpha)^2 + (x_b \cos\alpha - z)^2]^{3/2}}$$

$$= 2\int_{-\infty}^{0} z[\text{erf}(U_0 \cos\alpha - z \cot\alpha) + 1] \exp[-(z - U_0 \sin\alpha)^2]dz. \tag{A2}$$

APPENDIX B: THE FREE-MOLECULAR FORCE OVER A SPECULAR AIRFOIL

Considering the specular-wall system, the plate-ground setup may be conveniently replaced by a double-plate configuration, where the image plate is placed symmetrically about the ground, as depicted in Fig. 10. In line with the plate middle-point distance H from the ground, the two objects midchords are placed 2H apart, where the image plate is 2α -rotated relative to the airfoil. For convenience, we denote the axes coinciding with and normal to the physical plate by \tilde{x} and \tilde{y} , respectively, as introduced after Eq. (19) and marked in Fig. 10.

For the purpose of approximating the free-molecular specular-wall force over the airfoil, we take account only of particles that interacted a small number of times with the airfoil or its image prior to hitting the plate $\tilde{y} = 0^-$ lower side. This is expected to be a reasonable estimate in setups where the plate-ground distance H is nonsmall, as validated in Sec. V (see Fig. 9). Using the $(\tilde{x}, \tilde{y}, z)$ system of coordinates, we denote

$$f_{M_0} = \pi^{-3/2} \exp\left[-(\xi_{\tilde{x}} - U_0 \cos \alpha)^2 - (\xi_{\tilde{y}} - U_0 \sin \alpha)^2 - \xi_z^2\right],$$

$$f_{M_p} = \pi^{-3/2} \exp\left[-(\xi_{\tilde{x}} - U_0 \cos \alpha)^2 - (\xi_{\tilde{y}} + U_0 \sin \alpha)^2 - \xi_z^2\right],$$

$$f_{M_i} = \pi^{-3/2} \exp\left[-(\xi_{\tilde{x}} - U_0 \cos 3\alpha)^2 - (\xi_{\tilde{y}} - U_0 \sin 3\alpha)^2 - \xi_z^2\right],$$
and
$$f_{M_{ip}} = \pi^{-3/2} \exp\left[-(\xi_{\tilde{x}} - U_0 \cos 3\alpha)^2 - (\xi_{\tilde{y}} + U_0 \sin 3\alpha)^2 - \xi_z^2\right]$$
(B1)

to mark the Maxwellian velocity distributions of particles that have not interacted with either the plate or its image $[f_{M_0}]$; cf. Eq. (6)]; gotten reflected solely at the bottom part of the plate (f_{M_p}) ; emitted only at the upper part of the image body (f_{M_i}) ; or collided once with each surface, starting with the image plate and then with the airfoil $(f_{M_{ip}})$, respectively. The net effect of ground reflections on the airfoil aerodynamic force is quantitated by replacing the contributions of the nonconfined stream loading to the force with the mirror-plate reflections in pertinent velocity-space sections. Specifically, the approximate expressions for the ground contributions to the normal and tangential flow stresses at the plate lower surface are

$$\Delta P_{\tilde{y}\tilde{y}_{lp}} = \int_{0}^{\infty} \int_{c_{1}\xi_{\tilde{y}}}^{c_{2}\xi_{\tilde{y}}} \int_{-\infty}^{\infty} \xi_{\tilde{y}}^{2} (f_{M_{i}} - f_{M_{0}}) d\xi_{z} d\xi_{\tilde{x}} d\xi_{\tilde{y}} + \int_{-\infty}^{0} \int_{-c_{1}\xi_{\tilde{y}}}^{-c_{2}\xi_{\tilde{y}}} \int_{-\infty}^{\infty} \xi_{\tilde{y}}^{2} (f_{M_{ip}} - f_{M_{p}}) d\xi_{z} d\xi_{\tilde{x}} d\xi_{\tilde{y}} \quad \text{and} \quad \Delta P_{\tilde{x}\tilde{y}_{lp}} = \int_{0}^{\infty} \int_{c_{1}\xi_{\tilde{y}}}^{c_{2}\xi_{\tilde{y}}} \int_{-\infty}^{\infty} \xi_{\tilde{x}}\xi_{\tilde{y}} (f_{M_{i}} - f_{M_{0}}) d\xi_{z} d\xi_{\tilde{x}} d\xi_{\tilde{y}} + \int_{-\infty}^{0} \int_{-c_{1}\xi_{\tilde{y}}}^{-c_{2}\xi_{\tilde{y}}} \int_{-\infty}^{\infty} \xi_{\tilde{x}}\xi_{\tilde{y}} (f_{M_{ip}} - f_{M_{p}}) d\xi_{z} d\xi_{\tilde{x}} d\xi_{\tilde{y}},$$
(B2)

respectively, where

$$c_1 = \frac{\cos 2\alpha + 4H \sin \alpha - 2\tilde{x}}{\sin 2\alpha - 4H \cos \alpha} \quad \text{and} \quad c_2 = \frac{\cos 2\alpha - 4H \sin \alpha - 2\tilde{x}}{\sin 2\alpha + 4H \cos \alpha}.$$

Calculating the ξ_z integrals in Eq. (B2) explicitly, it remains to evaluate the $\xi_{\tilde{x}}$ and $\xi_{\tilde{y}}$ quadratures before computing the overall ground force. To this end, we introduce

$$I_{m,n}^{\stackrel{\infty}{=}} = \int_{0}^{\infty} \xi_{\bar{y}}^{m} [\text{erf}(U_{0} \cos n\alpha \pm c_{1} \xi_{\bar{y}}) - \text{erf}(U_{0} \cos n\alpha \pm c_{2} \xi_{\bar{y}})] e^{-(\xi_{\bar{y}} \pm U_{0} \sin n\alpha)^{2}} d\xi_{\bar{y}} \text{ and }$$

$$I_{m,n}^{\stackrel{0}{=}} = \int_{-\infty}^{0} \xi_{\bar{y}}^{m} [\text{erf}(U_{0} \cos n\alpha \pm c_{1} \xi_{\bar{y}}) - \text{erf}(U_{0} \cos n\alpha \pm c_{2} \xi_{\bar{y}})] e^{-(\xi_{\bar{y}} \pm U_{0} \sin n\alpha)^{2}} d\xi_{\bar{y}}, \tag{B3}$$

together with

$$J_{n}^{\pm} = \pm \frac{(U_{0} \sin n\alpha + c_{1}U_{0} \cos n\alpha) \exp\left[\frac{(c_{1}U_{0} \cos n\alpha + U_{0} \sin n\alpha)^{2}}{c_{1}^{2} + 1} - U_{0}^{2}\right] \left(\text{erf}\left[\frac{U_{0} \sin n\alpha + c_{1}U_{0} \cos n\alpha}{\sqrt{c_{1}^{2} + 1}}\right] + 1\right)}{4\sqrt{\pi}(c_{1}^{2} + 1)^{3/2}}$$

$$\mp \frac{(U_{0} \sin n\alpha + c_{2}U_{0} \cos n\alpha) \exp\left[\frac{(c_{2}U_{0} \cos n\alpha + U_{0} \sin n\alpha)^{2}}{c_{2}^{2} + 1} - U_{0}^{2}\right] \left(\text{erf}\left[\frac{U_{0} \sin n\alpha + c_{2}U_{0} \cos n\alpha}{\sqrt{c_{2}^{2} + 1}}\right] + 1\right)}{4\sqrt{\pi}(c_{2}^{2} + 1)^{3/2}}$$

$$\pm \frac{\exp(-U_{0}^{2})}{4\pi(c_{1}^{2} + 1)} \mp \frac{\exp(-U_{0}^{2})}{4\pi(c_{2}^{2} + 1)},$$
(B4)

through which

$$\Delta P_{\tilde{y}\tilde{y}_{lp}} = \frac{1}{2\sqrt{\pi}} \begin{pmatrix} \sum_{l=0}^{\infty} -I_{2,1}^{\infty} + I_{2,3}^{+} - I_{2,1}^{+} \\ I_{2,3}^{-} - I_{2,1}^{-} - I_{2,1} \end{pmatrix} \text{ and}$$

$$\Delta P_{\tilde{x}\tilde{y}_{lp}} = \frac{U_{0}\cos\alpha}{2\sqrt{\pi}} \begin{pmatrix} \sum_{l=0}^{\infty} -I_{1,1}^{\infty} + I_{1,3}^{+} - I_{1,1}^{+} \\ I_{0}^{-} - I_{0,1}^{-} - I_{1,1}^{-} \end{pmatrix} + J_{3}^{+} - J_{1}^{+} + J_{3}^{-} - J_{1}^{-}.$$
(B5)

In line with the above approximation, the integrals in Eqs. (B3) may be approximated by expanding the integrands about $H \gg 1$. Additionally, we consider small $\alpha \ll 1$ angles of attack, yielding, to a leading order

$$I_{1,n}^{\infty} \approx \pm \frac{2(2\tilde{x} - 1)}{\sqrt{\pi}H} \left[\frac{\sqrt{\pi}[2(U_0 n\alpha)^2 + 1]}{4} [1 \mp \operatorname{erf}(U_0 n\alpha)] \mp \frac{U_0 n\alpha e^{-(U_0 n\alpha)^2}}{2} \right],$$

$$I_{2,n}^{\infty} \approx \pm \frac{2(2\tilde{x} - 1)}{\sqrt{\pi}H} \left[\pm \frac{\sqrt{\pi}U_0 n\alpha[2(U_0 n\alpha)^2 + 3]}{4} [-1 \pm \operatorname{erf}(U_0 n\alpha)] + \frac{(U_0 n\alpha)^2 + 1}{2} e^{-(U_0 n\alpha)^2} \right],$$

$$I_{1,n}^{0} \approx \pm \frac{2(2\tilde{x} - 1)}{\sqrt{\pi}H} \left[\frac{\sqrt{\pi}[2(U_0 n\alpha)^2 + 1]}{4} [1 \pm \operatorname{erf}(U_0 n\alpha)] \pm \frac{U_0 n\alpha e^{-(U_0 n\alpha)^2}}{2} \right] \quad \text{and}$$

$$I_{2,n}^{0} \approx \pm \frac{2(2\tilde{x} - 1)}{\sqrt{\pi}H} \left[\pm \frac{\sqrt{\pi}U_0 n\alpha[2(U_0 n\alpha)^2 + 3]}{4} [-1 \mp \operatorname{erf}(U_0 n\alpha)] - \frac{(U_0 n\alpha)^2 + 1}{2} e^{-(U_0 n\alpha)^2} \right].$$
(B6)

A similar $H \gg 1$ and $\alpha \ll 1$ expansion may be carried out (yet is not necessary) for expressing J_n^\pm in Eq. (B4) to the same level of approximation. Substituting Eqs. (B6) and (B4) into Eq. (B5), the approximate expressions for the specular-wall force over the airfoil may be obtained through simple \tilde{x} integrations of $\Delta P_{\tilde{y}\tilde{y}_{lp}}$ and $\Delta P_{\tilde{x}\tilde{y}_{lp}}$ over the airfoil lower side and superposition with the known formulas for the free-stream loading [see Eqs. (19) and (20) et seq.]. The effectiveness of the above approximation is tested in Sec. V, where it is compared with the full free-molecular solution and DSMC finite-Knudsen predictions. Notably, the analytic expressions similarly support that free-molecular ground reflections invariably yield a positive contribution to the aerodynamic loading over the airfoil, thus increasing both lift and drag compared with their free-stream counterparts.

^[1] A. E. Raymond, Ground influence of aerofoils, NACA Technical Note No. 67, 1921.

^[2] I. G. Recant, Wind-tunnel investigation of ground effect on wings with flaps, NACA Technical Note No. 705, 1939.

^[3] E. G. Reid, A full-scale investigation of ground effect, NACA Technical Report No. 265, 1927.

^[4] S. Tomotika, T. Nagamiya, and Y. Takenouti, The lift on a flat plate placed near a plane wall, with special reference to the effect of the ground upon the lift of a monoplane aerofoil, Report No. 97, Aeronautical Research Institute, Tokyo Imperial University, Japan, 1933.

^[5] S. Tomotika, Z. Hasimoto, and K. Urano, The forces acting on an aerofoil of approximate Joukowski type in a stream bounded by a plane wall, Q. J. Mech. Appl. Math. 4, 289 (1951).

^[6] S. Widnall and T. Barrows, An analytic solution for two- and three-dimensional wings in ground effect, J. Fluid Mech. **41**, 769 (1970).

^[7] N. Hirata and Y. Kodama, Flow computation for three-dimensional wing in ground effect using multiblock technique, J. Soc. Nav. Archit. Jpn. 1995, 49 (1995).

- [8] C.-M. Hsiun and C.-K. Chen, Aerodynamic characteristics of a two-dimensional airfoil with ground effect, J. Aircr. 33, 386 (1996).
- [9] Z.-G. Yang, W. Yang, and Q. Jia, Ground viscous effect on 2d flow of wing in ground proximity, Eng. Appl. Comput. Fluid Mech. 4, 521 (2010).
- [10] J. Jung, H. Yoon, H. Chun, P. Hung, and O. Elsamni, Mean flow characteristics of two-dimensional wings in ground effect, Int. J. Nav. Archit. Ocean Eng. 4, 151 (2012).
- [11] J. R. Stadler and V. J. Zurick, Theoretical aerodynamic characteristics of bodies in a free-molecular-flow field. NACA Technical Note 2423, 1951.
- [12] C. Cercignani and M. Lampis, Free molecular flow past a flat plate in the presence of a nontrivial gassurface interaction, J. Appl. Math. Phys. 23, 713 (1972).
- [13] K. Aoki, K. Kanba, and S. Takata, Numerical analysis of a supersonic rarefied gas flow past a flat plate at an angle of attack, Phys. Fluids **9**, 1144 (1997).
- [14] Q. Sun, I. D. Boyd, and G. Candler, Numerical simulation of gas flow over microscale airfoils, J. Thermophys. Heat Transfer 16, 171 (2002).
- [15] Q. Sun and I. D. Boyd, Drag on a flat plate in low-Reynolds-number gas flows, AIAA J. 42, 1066 (2004).
- [16] Q. Sun and I. D. Boyd, Flat-plate aerodynamics at very low Reynolds number, J. Fluid Mech. 502, 199 (2004).
- [17] A. A. Abramov, A. V. Butkovskii, and O. Buzykin, Rarefied gas flow past a flat plate at zero angle of attack, Phys. Fluids 32, 087108 (2020).
- [18] J. Fan, I. D. Boyd, and C.-P. Cai, Computation of rarefied gas flows around a NACA 0012 airfoil, AIAA J. 39, 618 (2001).
- [19] A. Shoja-Sani, E. Roohi, M. Kahroma, and S. Stefanov, Investigation of aerodynamic characteristics of rarefied flow around NACA 0012 airfoil using DSMC and NS solvers, Eur. J. Mech. B: Fluids 48, 59 (2014).
- [20] C. Pekardan and A. Alexeenko, Rarefaction effects for transonic airfoil flows at low Reynolds numbers, AIAA J. 56, 765 (2018).
- [21] R. Shapiro and A. Manela, Thin-airfoil aerodynamics in a rarefied gas wind tunnel: A theoretical study, Phys. Fluids 36, 057107 (2024).
- [22] A. Ball, J. Garry, R. Lorenz, and V. Kerzhanovich, *Planetary Landers and Entry Probes* (Cambridge University Press, Cambridge, 2009).
- [23] F. Johnson, Lunar atmosphere, Rev. Geophys. 9, 813 (1971).
- [24] E. Lellouch, M. Belton, I. de Pater, G. Paubert, S. Gulkis, and T. Encrenaz, The structure, stability and global distribution of Io's atmosphere, Icarus 98, 271 (1992).
- [25] K. Khurana, W. McKinnon, and R. Pappalardo, Europa (University of Arizona Press, Tucson, 2017).
- [26] E. Musk, Hyperloop Alpha (2013), https://assets.sbnation.com/assets/3047069/hyperloop-alpha.pdf.
- [27] J. Braun, J. Sousa, and C. Pekardan, Aerodynamic design and analysis of the Hyperloop, AIAA J. 55, 4053 (2017).
- [28] K. Gkoumas, Hyperloop academic research: A systematic review and a taxonomy of issues, Appl. Sci. 11, 5951 (2021).
- [29] C. Gonzalez-Ballestero, M. Aspelmeyer, L. Novotny, R. Quidant, and O. Romero-Isart, Levitodynamics: Levitation and control of microscopic objects in vacuum, Science **374**, eabg3027 (2021).
- [30] Z. Lu, M. Stern, J. Li, D. Candia, L. Yao-Bate, T. J. Celenza, M. Azadi, M. F. Campbell, and I. Bargatin, Minimizing the ground effect for photophoretically levitating disks, Phys. Rev. Appl. 19, 044004 (2023).
- [31] B. Melo, M. Cuairan, G. Tomassi, N. Meyer, and R. Quidant, Vacuum levitation and motion control on chip, Nat. Nanotechnol. 19, 1270 (2024).
- [32] Y. Sone, Molecular Gas Dynamics: Theory, Techniques, and Applications (Birkhäuser, Boston, 2007).
- [33] C. Cercignani and M. Lampis, Kinetic models for gas-surface interactions, Transp. Theory Stat. Phys. 1, 101 (1971).
- [34] G. Bird, Molecular Gas Dynamics and the Direct Simulation of Gas Flows (Clarendon, Oxford, 1994).
- [35] W. Wagner, A convergence proof for Bird's direct simulation Monte Carlo method for the Boltzmann equation, J. Stat. Phys. 66, 1011 (1992).
- [36] A. Kuethe and C. Chow, Foundations of Aerodynamics (Wiley, New York, 1998).